Proceedings of FuelCell2008
Sixth International Fuel Cell Science, Engineering and Technology Conference
June 16-18, 2008, Denver, Colorado, USA

FUELCELL2008-65079

EFFECTS OF ELECTRODE MICROSTRUCTURE ON POLARIZATION CHARACTERISTICS OF SOFC ANODES

Yusuke Sakamoto, Naoki Shikazono, and Nobuhide Kasagi

The University of Tokyo
Department of Mechanical Engineering
Hongo 7-3-1, Bunkyo-ku, Tokyo, 113-8656, Japan

ABSTRACT

Anode microstructure parameters were quantified by SEM-EDX measurements and the dependence of polarization characteristics on the anode microstructure parameters is investigated experimentally. Nickel yttria-stabilized zirconia (Ni-YSZ) anode supported cells with a thin YSZ electrolyte, lanthanum-strontium-manganite(LSM)-YSZ composite cathode, and LSM cathode current collector layers were fabricated by dip coating method. Anode microstructure was successfully imaged and quantified by ultra low voltage SEM and by means of stereology. Cell voltage measurements and impedance spectroscopy were performed at 650 and 750˚C with hydrogen diluted by nitrogen as a fuel. A quantitative relationship between measured polarization and microstructure parameters, e.g., three phase boundary length, contiguity, etc., was discussed. Finally, a cell with an anode functional layer (AFL) was fabricated to investigate the possibility of improving both activation and concentration polarization characteristics.

1. INTRODUCTION

Solid Oxide Fuel Cell (SOFC) is one of the most promising energy conversion technologies due to its high efficiency and fuel flexibility. For cost reduction and high reliability, recent activities are shifting to achieve SOFC operation at intermediate temperatures (600~800˚C). In order to operate cells at such low temperature range, electrode polarization characteristics must be improved. Many researches reveal that electrode microstructure is crucial for polarization characteristics. In particular, anode microstructure has a large impact on total performance of anode-supported cells.

Great efforts have been made to improve anode performance by changing anode microstructures. For example, effects of grain and pore sizes[1][2][3], and difference of particle fabrication method[4] have been reported. However, anode microstructure parameters such as three phase boundary (TPB) length are not fully investigated yet, and the quantitative linkage between anode microstructure and its polarization losses remains unclear.

In the present work, the effects of anode microstructure on anode polarization are quantified and evaluated experimentally. To obtain cells with different anode microstructures, electrolyte, composite and current collector cathode layers were dip coated on anodes with different porosity and grain size. Then anode microstructures were imaged using scanning electron microscopy (SEM) with energy dispersive X-ray spectroscopy (EDX), and microstructure parameters were quantified by means of stereology. I-V curves and Cole-Cole plots were obtained by hydrogen experiments at temperatures of 650 and 750˚C. Finally, the relationship between the anode microstructure parameters and the polarizations are discussed.

2. EXPERIMENTS

2.1 Cell fabrication

Anode supported cells used in the present study consist of Ni-YSZ anode support (500 μm), YSZ electrolyte (~18 μm), LSM-YSZ composite (~10 μm) and LSM cathode current collector (~10 μm) layers. NiO-YSZ (60/40 vol.%) powders (AGC Seimi Chemical Co., Ltd.) with binder were mixed and extruded into a tube shape. After pre-sintering at 1100 or

Table 1. Cell fabrication parameters

Cell	Powder fabrication	Poreformer amount	Pre-sintering temperature
C-No poreformer	Co-precipitation	0 wt%	1200˚C
C-9wt%	Co-precipitation	9 wt%	1100˚C
C-17wt%	Co-precipitation	17 wt%	1100˚C
M-No poreformer	Mechanical mixing	0 wt%	1200˚C
M-9wt%	Mechanical mixing	9 wt%	1100˚C
M-17wt%	Mechanical mixing	17 wt%	1100˚C

1200˚C, a thin layer of YSZ was dip coated on the anode support, and sintered at 1400˚C for 3 hours. The LSM- YSZ (50/50 wt.%) composite cathode layer and LSM cathode current collector layer were dip coated and sintered at 1200 and 1100˚C for 3 hours, respectively. Finally, Ag wire was connected to the cell by Ag paste. Figure 1 shows the schematic of the fabricated anode supported cell.

To change anode porosity, the amount of acrylic poreformer (1.5 μm, Soken Chemical & Engineering Co., Ltd.) were varied as 0, 9 and 17 wt%. For original NiO-YSZ powders, mechanically mixed or co-precipited powders were employed. The mean grain size of the mechanically mixed powders was 1 μm. Primary particle size of the co-precipitated powders is 30~50 nm order and they were uniformly distributed inside the secondary grains of ~μm order size. Table 1 shows the cells used in this study. Figure 2 illustrates the cross section of fabricated cell.

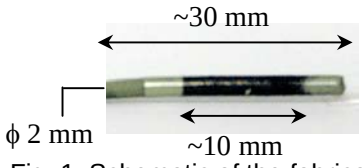

Fig. 1. Schematic of the fabricated cell

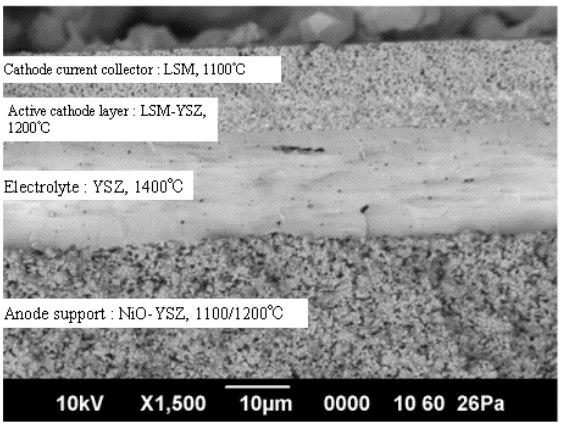

Fig. 2. Cross section of the fabricated cell

2.2 Anode microstructure quantification

The porous anode was fractured and impregnated with epoxy resin (Marumoto struers K. K.). Resin completely filled up the pores under vacuum. After hardening the resin, samples were polished by Ar-ion beam cross-section polisher (JEOL Ltd., SM-09010). This technique provides less damage and smoother cross section than mechanical polishing. Then, microstructure of the cross-section was successfully imaged by the ultra low voltage scanning electron microscopy (Carl Zeiss, ULTRA55) and energy dispersive X-ray spectroscopy (Thermo Electron, NSS300). Energy and angle selected backscattered electron detector provided images with very high resolution. Original SEM-EDX images were processed to distinguish Ni, YSZ and pore phases. Figure 3 shows the original and the processed images. From these processed images, following parameters are calculated.

Size d_i (Diameter of each phase) ;

$$d_i = 2\sqrt{\frac{A_i}{\pi}}, \quad (1)$$

shape R_i (Circularity of each phase) ;

$$R_i = \frac{P_i^2}{4\pi A_i}, \quad (2)$$

interfacial area $S_{i\text{-}j}$ (Neck area between phases) ;

$$S_{i-j} = 2N_{i-j}, \quad (3)$$

and TPB length L_{TPB} (Edge among three phases) ;

$$L_{TPB} = 2N_{TPB}, \quad (4)$$

where i and j denote each of the Ni, YSZ or pore phases. A_i is the area of each phase, P_i is the perimeter of each phase, $N_{i\text{-}j}$ is the number of contact points of i and j phases per unit length, N_{TPB} is the number of intersection points of three phases per unit area. These values can be directly obtained from the image analysis. Interfacial area $S_{i\text{-}j}$ which is the neck area between i and j phases per unit volume, and TPB length L_{TPB} are calculated from Eqs.(3) and (4), i.e., quantitative stereology. According to Gurland[5] and Underwood[6], the microstructural information from 2D images can be transformed to 3D structural information. Interfacial area between same phases $S_{i\text{-}i}$ cannot be directly obtained from the image, since $N_{i\text{-}i}$ is not identifiable. Thus, $S_{i\text{-}i}$ is obtained using contiguity $C_{i\text{-}j}$[6], which is defined as the fraction of the interfacial area of i and j phases to the total interfacial area of all phases, as follows;

$$C_{i-i} = \frac{2S_{i-i}}{2S_{i-i} + S_{i-j} + S_{i-k} + 2S_{j-j} + S_{j-k} + 2S_{k-k}}, \quad (5)$$

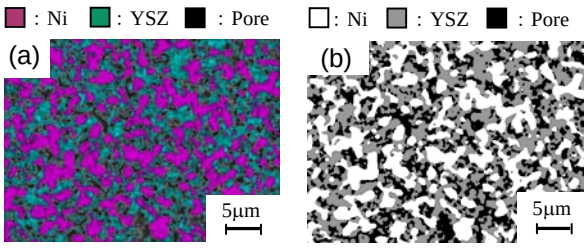

Fig.3. SEM-EDX images, (a) Original, (b) After processed (C-No poreformer cell)

$$2C_{i-i} + C_{i-j} + C_{i-k} \equiv C_i = \frac{V_i l_j l_k}{V_i l_j l_k + V_j l_k l_i + V_k l_i l_j}, \qquad (6)$$

where V_i is the volume fraction of each phase, l_i is the mean intercept length of each phase. Both V_i and l_i are available directly from the image. The ohmic resistance will be related to contiguity C_i in the later section.

2.3 Cell testing

The cells were connected to the fuel supply tube with Thermeez Hi-Seal and Dura Seal 1529 UHT (Cotronics Corp.) for adhesion bond and sealant. Ag wire was connected to the electronic load controller (Kikusui Electronics Corp., PLZ664) and impedance meter (Kikusui Electronics Corp., KFM2150).

The cells were reduced at 750˚C with hydrogen diluted by nitrogen for an hour. Hydrogen and nitrogen flow rates were set as 20/10 sccm or 2/28 sccm fixing the total flow rate constant. Air flow rate was fixed as 20 slm. Then, I-V curves and Cole-Cole plots were acquired at temperatures of 650 and 750˚C.

3. RESULTS AND DISCUSSION

3.1 Microstructure quantification results

Figure 4 shows the size d_i, shape R_i, and interfacial area S_{i-j} of the each phase. For co-precipitated cells, Ni and YSZ are nearly the same size (1.5 μm ~ 2.0 μm) and the YSZ shape is more complicated than Ni. On the contrary, for mechanically mixed cells, Ni size is much larger than YSZ, and Ni shape is more complicated. Furthermore, co-precipitation cells show larger YSZ-YSZ, Ni-YSZ and YSZ-pore interfacial area, while mechanically mixed cells show larger Ni-pore interfacial area. These results indicate that good connections of YSZ-YSZ and Ni-YSZ phases are achieved in co-precipitation cells, while Ni phase is relatively isolated in the pore and Ni can be easily agglomerated in mechanically mixed cells. Figure 5 shows the porosity and TPB length L_{TPB}. Good connections of YSZ-YSZ and Ni-YSZ phases in co-precipitated cells lead to high porosity and long TPB length.

3.2 Cell test results

Obtained voltage and power density curves are shown in Fig. 6. As shown in Fig. 6, all cells show better performance in H_2=20 sccm case, and the maximum power density (MPD) was over 0.4 W/cm^2 with C-No poreformer cell. Co-precipitated cells show better performance than mechanically mixed cells for H_2=2 sccm case. Especially, C-9wt% cell exhibits MPD of 0.15 W/cm^2 and maximum flow utilization exceeds 85%. The cells with 17 wt% poreformers show low open circuit voltage (OCV). The electrolyte layers of these cells seem not to be dense enough for perfect sealing.

To separate ohm, activation, and concentration polarizations, Cole-Cole plots were obtained. Figure 7 shows one of the obtained Cole-Cole plots. Two semi-circles were least-square fitted to obtain R_{ohm}, R_h and R_l resistances.

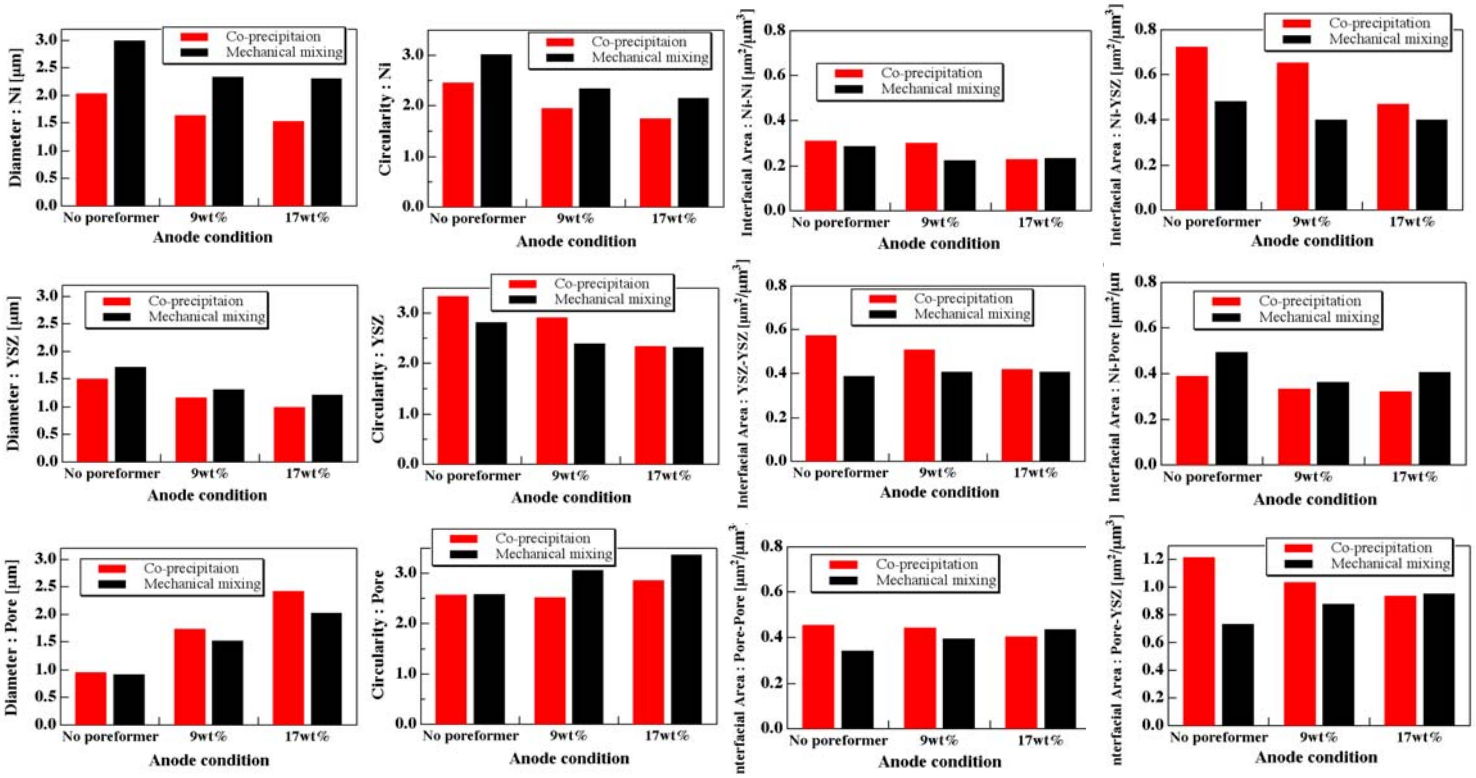

(a) Size (b) Shape (c) Interfacial area

Fig.4. Microstructure parameters

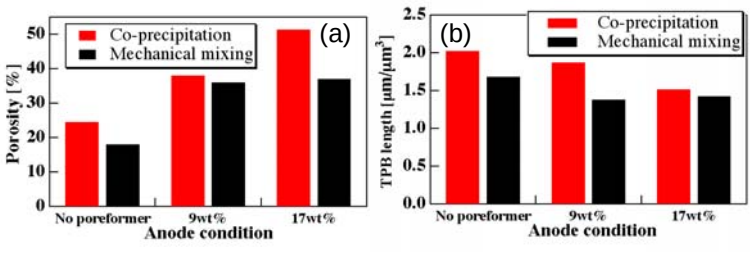

Fig. 5 Microstructure quantification results, (a) Porosity, (b) TPB length

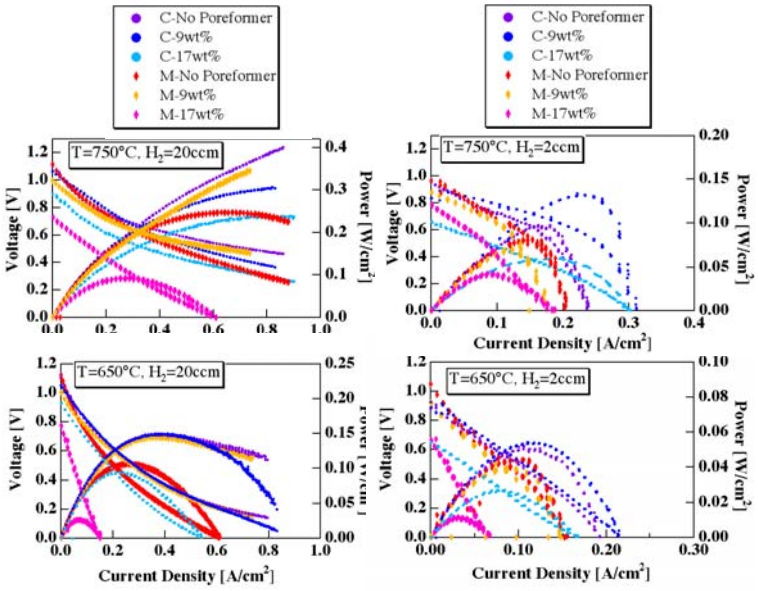

Fig. 6. Voltage and power density curves

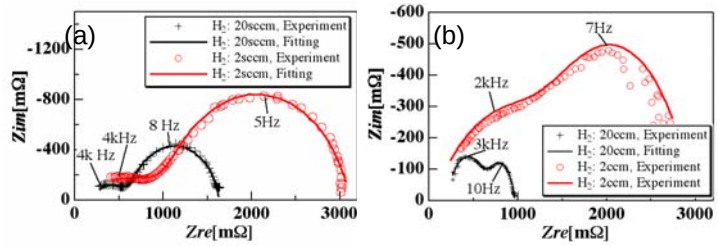

Fig. 7. Obtained Cole-Cole plots at 0.10A, (a) C-No poreformer, (b) C- 9wt%

The sum of the ohmic resistances of electrolyte, anode and cathode are measured as R_{ohm}. The high frequency resistance R_h is considered as the activation polarizations of anode and cathode[7]. The major contribution of the low frequency resistance R_l is due to the anode concentration polarization. Figure 8 shows the obtained R_h and R_l. R_h is dominant at 650˚C because of low catalyst activity at low temperature. On the contrary, R_l becomes dominant for small H_2 flow rate because of the low partial pressure of H_2 at TPB. As the amount of poreformer increases, a trade-off between increasing R_h and decreasing R_l arises. The C-9wt% cell performs best for this trade-off. In addition, at small H_2 flow rates, R_l is relatively low and depends on porosity for co-precipitated cells, while R_l is large and independent on porosity for mechanically mixed cells.

Polarization and Microstructure

Relationship between polarizations (R_{ohm}, R_h, and R_l) and microstructure parameters is discussed. According to the cc-theory[8], the ohmic resistance (σ) of a multi-phase material can be expressed as follows:

$$\sigma = \sum \sigma_i C_i V_i, \qquad (7)$$

where σ is the conductivity of the porous material, σ_i, C_i and V_i are the conductivity, contiguity and volume fraction of phase i, respectively. In the present case, i is applied only for the Ni phase. The value of σ_{Ni} is obtained from Tambrini[9] and C_{Ni} and V_{Ni} are calculated from the image analysis. Figure 9 shows the R_{ohm} obtained from Cole-Cole plots and R_{ohm} calculated from cc-theory. The value of σ_{YSZ} and σ_{LSM} is obtained from Ferguson[10] and Kiatkittipong[11]. As shown in Fig. 8, cc-theory can predict the trend of R_{ohm} quite well. Ohmic resistance R_{ohm} increases with porosity, but the increment is less than 100 mΩ, which is much smaller compared to the whole polarization.

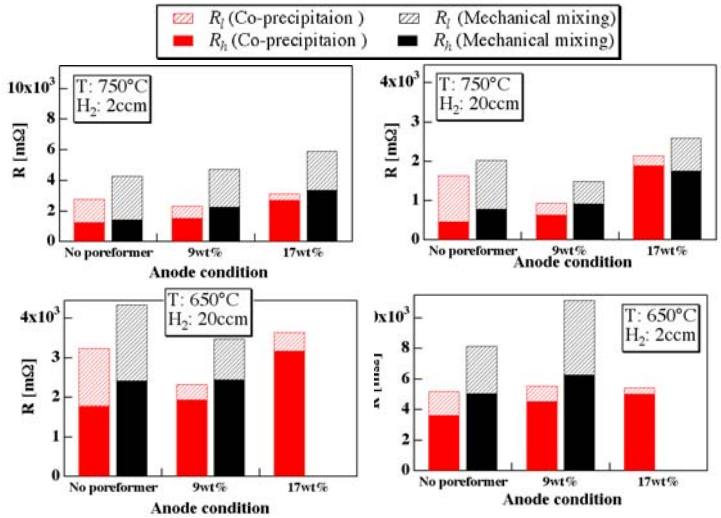

Fig. 8. R_h and R_l calculated from Cole-Cole plot with hydrogen of 20sccm, 2sccm at temperatures of 650, 750˚C

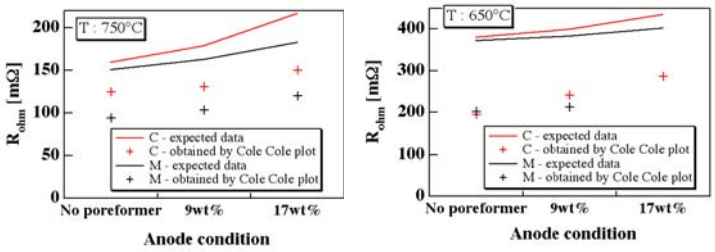

Fig. 9. R_{ohm} obtained from Cole-Cole plot from cc-theory

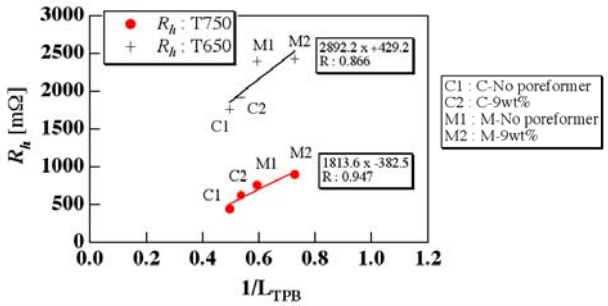

Fig.10. R_h obtained from Cole-Cole plot and TPB length by image analysis

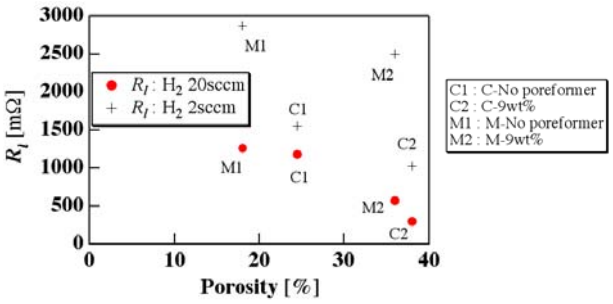

Fig. 11. R_l obtained from Cole-Cole plot and porosity by image analysis

Figure 10 shows the high frequency polarization R_h against the reciprocal of TPB length from image analysis. As shown in Fig. 10, R_h is almost in inverse proportion to TPB length. This can be explained by the linearized Butler Volmer equation.

$$\eta_{act} = \frac{RT}{2Fi_0 L_{TPB}} i \qquad (8)$$

Figure 11 shows the low frequency polarization R_l against porosity. As shown in Fig. 11, R_l decreases as porosity increases. Mechanically mixied cells, however, exhibit higher R_l than co-precipitated cell at H_2=2 sccm case. This may be attributed to the poor connection of solid phases in mechanically mixed cells. Magnified images of the microstructure are shown in Fig. 12. Extremely narrow pores can be found between Ni and YSZ phases in mechanically mixed cell.

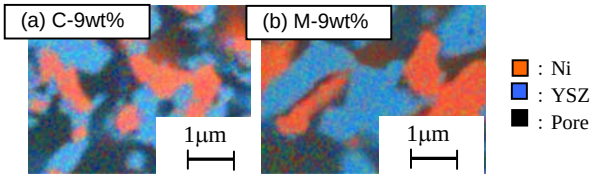

Fig. 12. Magnified images of co-precipitated and mechanically mixed cells, (a) C-9wt%, (b) M-9wt%

This indicates that tortuosity factor of mechanically mixed cells should be much higher than that of co-precipitated cells.

Anode function layer

As mentioned above, a trade-off arises between R_h and R_l. To decrease the total polarization (R_h + R_l), anode function layer (AFL) is put between the anode support and the electrolyte. C-9wt% cell which has the largest porosity is used for the anode support, and C-No poreformer slurry which has the longest TPB length is used for AFL. Figure 13 shows the microstructure of cell with a AFL.

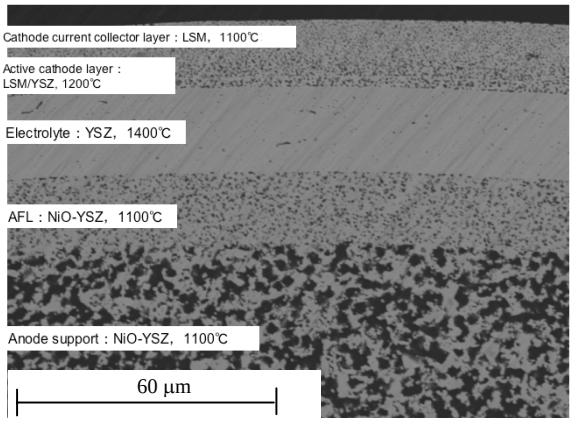

Fig. 13. Microstructure of AFL cell

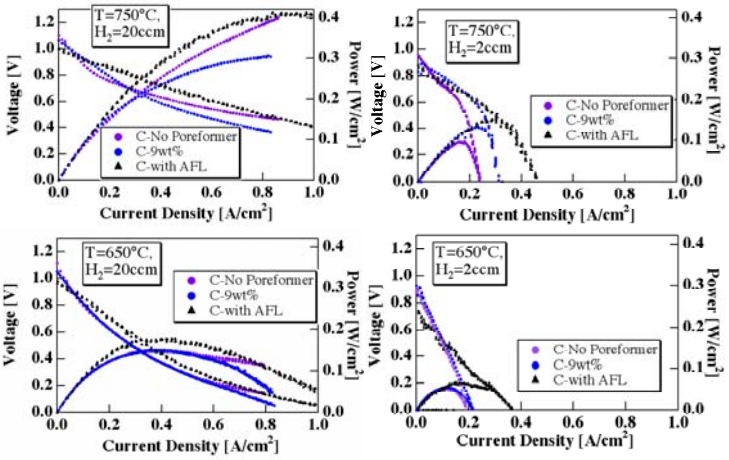

Fig. 14. Voltage and power density curves of cell with AFL

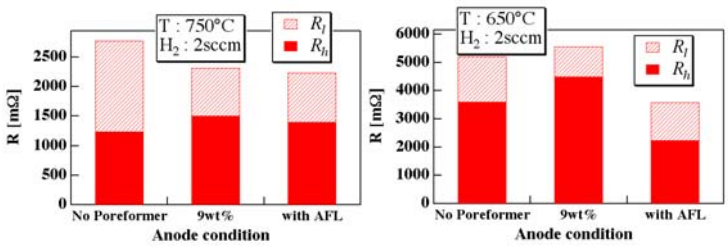

Fig. 15. R_h and R_l of cell with AFL

Figure 14 shows the voltage and power density curves of C-No poreformer, C-9wt%, and AFL cells. As shown in Fig. 14, AFL cell shows better performance. At 750℃ with low H_2=2 sccm, maximum fuel utilization of AFL cell is nearly 95%, which is about 10% larger than that of C-9wt% cell. Figure 15 shows R_h and R_l obtained from Cole-Cole plot. As shown in Fig. 15, sum of R_h and R_l of AFL cell is lower for both conditions. R_l of AFL is nealy the same as C-9wt% cell. It is emphasized that R_h of AFL cell at 650˚C, H_2=2 sccm become much smaller than that of C-No poreformer cell. R_h is improved because of the partial pressure dependence of exchange current density. This indicates that AFL layer can effectively decrease the amount of R_h and R_l at high fuel utilization conditions.

CONCLUSIONS

In the present study, tubular anode-supported cells with Ni-YSZ anode, YSZ electrolyte, LSM-YSZ composite cathode, and LSM cathode current collector layers were fabricated. Amount of acrylic poreformer was changed and different NiO-YSZ powders were used to obtain different anode microstructures. Anode microstructure was successfully imaged with CP and SEM-EDX. Clear images of ultra low voltage SEM-EDX made it possible to quantify microstructure parametes. Co-precipitated cells have good connection of Ni-YSZ and YSZ-YSZ phases which leads to high porosity with long TPB length. On the other hand, in mechanically mixed cells, Ni is isolated in the pore and TPB length and porosity are small. Electrochemical performance was measured at 650 and 750˚C with hydrogen diluted by nitrogen. Ohmic polarization can be well predicted by the cc-theory. Activation polarization is nearly in inverse proportion to the TPB length. Concentration polarization correlated well with the porosity. But tortuosity factor of sub-micrometer level should be taken into account. Finally, a cell with anode functional layer (AFL) was fabricated which successfully reduced both activation and concentration polarizations.

ACKNOWLEDGEMENTS

This research was supported through the 21st Century COE Program, “Mechanical System Innovation,” by the Ministry of Education, Culture, Sports, Science and Technology of Japan (MEXT). We would like to thank AGC Seimi Chemical Co., Ltd., Kankyo Ceramics Research Co., Ltd. and Showa Shell Sekiyu K. K. for supplying original powders and extruded tubes and for the beneficial discussions.

REFERENCES

[1] H, Koide *et al*., 2000, “Properties of Ni/YSZ cermet as anode for SOFC,” *Solid State Ionics*, **132**, pp. 253-260.

[2] T, Fukui *et al*., 2001, “Morphology and performance of SOFC anode fabricated from NiO/YSZ composite particles,” *J. Chemical Engineering of Japan*, **34**, pp. 964-966.

[3] Y, Yamaguchi, N, Shikazono, 2007, “Research on Anode Microstructures and Polarization Characteristics of Anode Suported Solid Oxide Fuel Cell,” *Proc. JSME Annual Meeting*, **(3)**, pp. 67-68.

[4] S, -D. Kim *et al*., 2006, “Performance and durability of Ni-coated YSZ anodes for intermediate temperature solid oxide fuel cells,” *Solid State Ionics*, **177**, pp. 931-938.

[5] J, Gurland, 1966, “An estimate of Contact and Contiguity of Dispersions in Opaque Samples,” *Trans. Metallurgical Society of AIME*, **236**, pp. 642-646.

[6] E, E, Underwood, 1972, “Stereology and quantitative metallography,” *Philadelphia: American Society for Testing Materials.*

[7] R, Barford *et al*., 2007, “Detailed characterization of anode-supported SOFCs by impedance spectroscopy,” *J. Electrochem. Soc*., **154** (4), pp. B371-B378.

[8] D, Simwonis, F, Tietz and D, Stover, 2000, “Nickel coarsening in annealed Ni/8YSZ anode substrates for solid oxide fuel cells,” *Solid State Ionics*, **132**, pp. 241-251.

[9] U, Anselmi-Tamburini *et al*., 1998, “Electrical properties of Ni/YSZ cermets obtained through combustion synthesis,” *Solid State Ionics*, **110**, pp. 35-43.

[10] J, R, Ferguson *et al*., 1996, “Three-dimensional numerical simulation for various geometries of solid oxide fuel cells,” *J. Power Sources*, **58**, pp. 109-122.

[11] W, Kiatkittipong *et al*., 2005, “Oxygen transport through LSM/YSZ/LaAlO system for use of fuel cell type reactor,” *Chem. Eng. J*., **106**, pp. 35-42.